

Highlights

Considerations for massic activity determination by Decay Energy Spectrometry (DES) using cryogenic Transition Edge Sensors (TES)

B. Alpert, D.E. Bergeron, M. Carlson, R. Fitzgerald, S. Jollota, S. Muramoto, S. Nour, G. O'Neil, D. Schmidt, R. Verkouteren

- Absolute massic activity of ^{243}Am by Decay Energy Spectrometry
- Traceable preparation of microgram sources by drop-on-demand inkjet gravimetry
- Identifying and quantifying radionuclide impurities by multi-nuclide fit of DES spectrum to Monte Carlo model
- Methods for total event counting with live-timed absolute activity and integral based loss-free pulse correction

Considerations for massic activity determination by Decay Energy Spectrometry (DES) using cryogenic Transition Edge Sensors (TES)

B. Alpert^a, D.E. Bergeron^a, M. Carlson^a, R. Fitzgerald^a, S. Jollota^a, S. Muramoto^a, S. Nour^a, G. O'Neil^a, D. Schmidt^a, R. Verkouteren^a

^a*National Institute of Standards and Technology, 100 Bureau Dr, Gaithersburg, 20899, MD, USA*

Abstract

Decay Energy Spectrometry (DES) using cryogenic Transition Edge Sensors (TES) is a promising technique for activity standardization due to its 4π geometry, high absorption efficiency, high energy resolution, and low background. This enables DES to identify and quantify radionuclides, including impurities that are difficult to quantify simultaneously by other methods, without the need for chemical separations. For DES to be used as a primary standardization method, it is necessary to ensure accurate deposition of microgram amounts of source solution and to eliminate bias from pulse pileup or pulse shape variability. To address these challenges, we have developed new methods for DES sample preparation, TES chip design, and data analysis. We present massic activity and isotopic ratio results for ^{243}Am sources with ^{241}Am impurity, live-timing with extending dead time and pileup exclusion, and correction of systematic errors due to data acquisition challenges unique to DES. We show that after these considerations are made, relative combined standard uncertainties below 1% are achievable. The ^{243}Am massic activity determined by DES agrees well with the value determined by liquid scintillation (LS) counting, with the ratio of the two values and its combined uncertainty $A_{\text{DES}}/A_{\text{LS}} = 1.000 \pm 0.005$.

Keywords: Decay Energy Spectrometry (DES); Transition Edge Sensor (TES); Mass metrology; Drop-on-demand inkjet gravimetry; primary measurement; Americium-243; alpha emitter

1. Introduction

The importance of cryogenic calorimetry in radionuclide metrology has been increasingly recognized since the CCRI(II) intercomparison of ^{241}Pu activity [1], wherein several participants evaluated the effect of the adopted beta spectrum on the LS efficiencies used in their activity determinations. Participants noted improved between-method agreement when using shape factors approximating the experimental beta spectrum measured by Loidl et al. with cryogenic calorimeters [2]. There has been a focus on improved beta spectra [3, 4, 5, 6] and their incorporation into LS counting efficiency models [7, 8, 9, 10]. At the same time, cryogenic calorimetry is increasingly considered promising as the basis for new, independent absolute activity measurements [11, 12, 13, 14, 15, 16].

This work focuses on massic activity measurements of ^{243}Am in solution. The radionuclide ^{243}Am is not found in nature and is artificially produced primarily in the nuclear fuel cycle through neutron capture on ^{242}Pu , from the beta decay of ^{243}Pu , and successive neutron absorption of ^{241}Am . It may be used as a tracer in isotope dilution analysis, as a radiochemical separation yield tracer [17], for nuclear safeguards monitoring [18, 19], and rarely in smoke detectors. It has a half-life of (7364 ± 22) years and decays by alpha particle emission to ^{239}Np [20]. This study has been carried out in parallel with the production of a new ^{243}Am radioactivity standard reference material (SRM) by NIST; details regarding the primary solution and standardization by established methodology are presented in [21]. We determine absolute massic activity and impurity ratios for the ^{243}Am solution using Decay Energy Spectrometry (DES), showing agreement with other methods within estimated uncertainties. The DES method is unique among the other methods used in the SRM certification (liquid scintillation, alpha spectrometry, mass spectrometry, gamma-ray spectrometry), in that it provides activity of multiple radionuclides without the need of chemical separation, tracers, or activity calibration standards.

In DES, radioactive material is fully enclosed in an absorber, and the energy released by each radioactive decay is thermalized and measured by a sensitive thermometer. DES using cryogenic detectors [22] provides the advantages of high energy resolution combined with 4π detection geometry and ideally 100% efficiency for alpha particles. Two commonly used cryogenic detectors are Transition Edge Sensors (TES) and Metallic Magnetic Calorimeters (MMC). DES measurements of absolute activity with high re-

solving power have been carried out using MMCs [13, 23]. MMCs have been used to determine absolute X-ray emission intensities for ^{241}Am by determining both activity and x-ray intensities in one measurement [24]. Low energy beta spectrometry has been carried out using MMCs [25] and cryogenic thermistors [26], with TESs also capable of the necessary resolution [27]. The method of DES source preparation plays a large role in energy resolution [28, 29, 23, 30], with common techniques including nanoporous substrates to minimize formation of crystals and diffusion welding to improve thermal conductivity.

We use Transition Edge Sensors (TES) as cryogenic calorimeters due to NIST expertise in TES fabrication and due to the versatility of the device allowing it to be tailored to a specific energy range and pulse speed [31, 32]. NIST-manufactured TES chips similar to the ones described in the present work have been used to measure the $^{240}\text{Pu}/^{239}\text{Pu}$ isotopic mass ratio validated by mass spectrometry [29], demonstrating 1 keV FWHM at 5.5 MeV. Multi-nuclide analysis of ^{227}Ac impurity in ^{225}Ac with similar TES chips has also been carried out [33]. Because we are focused on absolute activity, we develop data analysis techniques specific to our detectors for accurate pulse counting. In spectroscopic or relative activity applications, an approach such as optimal filtering is likely to give the highest energy resolution spectrum [34, 35], once pulses not matching a standard shape are discarded. To include more pulses in the spectrum, algorithms based on a running sum have been developed such as discussed in [36, 37]. For our application, extending live time correction is applied when pulses need to be discarded.

DES requires the use of low activity (≈ 10 Bq) sources that are also physically small (≈ 1 mm). Maintaining a gravimetric link between primary solution and DES sources that contain approximately 60 μg of solution each, is therefore a key step in this work. We use an automated inkjet device, for which we have demonstrated uncertainties below 1% [38]. We recently completed a validation of the inkjet gravimetric link with an overall combined standard uncertainty less than 1% and potential losses of radioactive material of $(0.017 \pm 0.018)\%$ [15]. In the present work, we again confirm the inkjet-deposited masses by LS counting of samples made by pycnometer and inkjet dispensing.

2. Experimental Methods

2.1. Overview

Gravimetrically linked sources were prepared (Sections 2.2 and 2.3) for absolute massic activity measurements by decay energy spectrometry (DES). Liquid scintillation (LS) counting (Sections 2.4 and 2.5) provided a check of the gravimetry methods [38, 15, 39]. Sources for DES were prepared on nanoporous gold foil substrates (Section 2.6) and measured using transition edge sensors designed for our application (Section 2.7).

2.2. Gravimetric source preparation scheme

All sources were prepared from a carrier-free 1 mol/L HNO₃ stock solution of ²⁴³Am, with massic activity of approximately 20 kBq/g [21]. Using methodology described previously [15, 39], liquid scintillation (LS) sources were prepared by pycnometer from the stock solutions before filling the inkjet reservoir and after inkjet dispensing, providing a check for evaporative concentration of the solution during the inkjet experiment. LS sources were also prepared by inkjet deposition of N_{vial} drops into vials with LS cocktail; comparing the massic LS count rates of pycnometer- and inkjet-dispensed LS sources provides a precise radiometric check of the inkjet gravimetry. The DES sources were bracketed by LS sources prepared by inkjet, providing a check of the inkjet stability. Inkjet drop mass calibrations by microbalance were carried out throughout the experiment. This scheme is represented in Figure 1(a).

Planning for inkjet drop mass $m_d \approx 65$ ng, $N_{\text{foil}} = 1144$ drops were programmed to be deposited onto each DES sample foil, targeting ≈ 1.5 Bq each. A Microfab Technologies Jetlab 4 microdeposition system with a 60 μm piezoelectric device (MJ-AB-OIL-60-8MX) was used to eject a programmed number of drops of ²⁴³Am solution into LS vials (N_{vial}) and onto DES foils (N_{foil}). The barb of the device had been sputtered with a layer of gold for protection from corrosion. A jig was constructed that held a sample slide at the same height as four vials containing scintillation fluid (Figure 1(a)) to minimize vertical movement of the device.

Two inkjet passes were used with different shapes of DES foils. Smaller size foils have a better signal to noise ratio, while larger size foils prevent the deposited solution from reaching the foil edges and causing partial energy deposition in the absorber. Pass 1 foils were laser-cut to 2.4 mm by 2.45 mm rectangles and laser-etched to facilitate folding in an envelope-like shape.

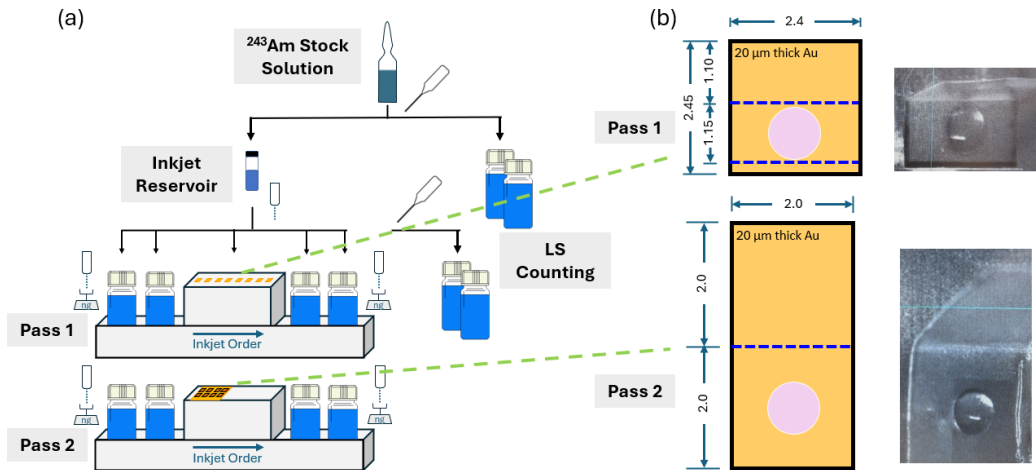


Figure 1: (a) Experimental-design including liquid scintillation sources prepared by pycnometer before and after inkjet printing and by inkjet before and after deposition of DES sources. The sample holder is illustrated with the Pass 1 and Pass 2 foils, with inkjet order from left to right, bracketing each pass of DES sources by 2 LS vials and drop mass calibrations. In Pass 1, the slide held individual foils fixed onto gels in a linear array. In Pass 2, the slide held a template of foils to simplify alignment; the template was cut into individual samples following deposition. (b) The dimensions of foils in mm, illustrating outer cut edges (black outline), inner etch lines for folding (blue dashed lines), and approximate location of inkjet deposition drop on the foil (pink circle). Photos from the inkjet camera show the deposited drop on pre-folded Pass 1 and Pass 2 foils.

Pass 2 foils were laser-cut to 2 mm by 4 mm rectangles and laser-etched to facilitate folding in half. Foils were pre-folded to $\approx 90^\circ$ along the etched lines to reduce handling after deposition, and arranged on gel substrates which served as placemats for the inkjet deposition. An identical foil was also placed on the gel during the inkjet deposition to serve as a matched blank. The inkjet was aligned to deposit on the ≈ 1 mm diameter target location illustrated in Figure 1(b).

The inkjet-deposited solution on the foils dried within seconds. Dried foils were folded with tweezers, taking care not to touch the nanoporous side that had received the activity. The folded foils were then placed between polished stainless steel plates and rolled in a manual rolling mill to compress the foils together. The foils were then thermally connected to a TES chip for measurement.

2.3. Drop Mass Calibration

The mass of the dispensed drops m_d was measured by two independent methods (Method 1 and Method 2). Method 1 measures the mass rise of a vessel on a microbalance inside the inkjet enclosure. The inkjet device was positioned over a gold-coated glass weighing vessel (8 mm by 20 mm) protected by an aluminum draft shield with a 3 mm hole drilled in the top of the shield. The weighing vessel was filled with 1 mol/L HNO₃ to within 3 mm of the top. The nozzle of the device was lowered through the hole in the draft shield so that the tip of the nozzle was level with the top of the weighing vessel. 5 000 drops were dispensed at 300 Hz to precondition the system and establish a steady evaporation rate from the weighing vessel. Then, a burst of $N_b = 10\,000$ drops was dispensed at $f = 300$ Hz.

After the evaporation rate reestablished itself, the two evaporation trends were extrapolated to a common midpoint, where the difference in the extrapolated values was divided by N_b to get the average mass of a drop (Burst procedure). This value was then compared to the drop mass calculated from the rising slope of the timestamped mass data (corrected for evaporation) during the drop ejection divided by the ejection rate f (Riserate procedure).

The Burst procedure is described by Eq. 1 where m_f and m_i are the microbalance readings before and after the burst, corrected for evaporation to a common time, and N_b is the number of drops in the burst.

$$m_d = \frac{m_f - m_i}{N_b} \quad (1)$$

The Riserate procedure is described by Eq. 2 where R_r is the massic rise rate, R_e is the massic evaporation rate, and f is the dispensing frequency.

$$m_d = \frac{R_r + R_e}{f} \quad (2)$$

Method 2 compares the LS count rate between vials prepared by inkjet deposition and by traditional pycnometer dispensing. The LS vials provide a means to calculate drop mass from the number of drops dispensed into the vial (here, $N_{\text{vial}} = 57\,200$, known exactly) and the LS count rate. This method requires several days of counting with uncertainties arising from counting statistics and the ability to avoid uncompensated evaporation during pycnometer manipulation. Assuming that the massic activity of the solution is constant throughout the experiment, this method is described by Eq. 3

where m_p is the mass of solution dispensed by pycnometer into the LS source, $R_{\text{LS-p}}$ is the net LS count rate for the pycnometer-prepared source, $R_{\text{LS-i}}$ is the net LS count rate for the inkjet-prepared LS source, and N_{vial} is the number of drops dispensed by inkjet into the LS source.

$$m_d = \frac{m_p \cdot R_{\text{LS-p}}}{R_{\text{LS-i}} \cdot N_{\text{vial}}} \quad (3)$$

2.4. Liquid Scintillation source composition

All LS sources were prepared in 22 mL glass vials with 20 mL Ultima Gold (PerkinElmer, Boston, MA, USA) and 1 drop (≈ 15 mg) of di-(2-ethylhexyl)phosphoric acid (HDEHP), a complexing agent that stabilizes Am in the cocktail. LS sources were prepared by pycnometer from the stock solution before inkjet dispensing, and from the solution remaining in the inkjet reservoir after dispensing. Each pycnometer-prepared LS source received approximately 0.05 g (≈ 1 kBq of ^{243}Am) of the stock solution. In addition, after the DES foils were removed, gel placemats from under the foils were added to LS vials containing 20 mL Ultima Gold and HDEHP, providing a check for stray activity from possible satellite drops, seepage off of the nanoporous foils, or leakage through the laser-etched fold lines.

2.5. Liquid Scintillation Counting

All LS sources were counted on a PerkinElmer Tri-Carb 4910 TR (PerkinElmer, Boston, MA, USA) and a PerkinElmer 1220 Quantulus; a subset were also counted on the NIST triple-to-double coincidence ratio (TDCR) counter [40]. Matched blanks were also prepared and counted for background subtraction.

2.6. DES substrates

The gold foils are 20 μm thick with a thin (≈ 2.5 μm) nanoporous layer to inhibit the formation of large crystals that would degrade DES energy resolution [29, 13, 23, 30, 41]. This effect was ascertained by SEM visualization of inkjet-deposited samples on porous and non-porous surfaces (see Supplement Figure 11). The nanoporous layer was comprised of a 10 nm Ti adhesion layer, a 100 nm Au layer, and a ≈ 2.4 μm Au and Ag alloy deposited through co-sputtering of Au and Ag targets in DC and RF modes at 1.2 A and 300 W, respectively, using a magnetron-based sputtering system (Denton Vacuum Explorer, Moorestown, NJ). The Au-Ag layer was de-alloyed in 14.4 mol/L nitric acid overnight. The resulting film had an average pore diameter of (44 ± 13) nm, and a porosity of approximately 21 % as determined

using SEM. Given the large volume of deposited solution, and to prevent any spillover or migration of the deposit during drying, hydrophobic patterns were created on the surface of the nanoporous layer. This was done by first immersing the substrate in a 1 mmol/L suspension of dodecanethiol (Sigma-Aldrich) in 200 proof ethyl alcohol for 1 minute, drying, and subsequent ion etching of the self-assembled monolayer in 1 mm squares using a 20 keV $\text{Ar}_{2800\pm 1000}$ cluster source at an ion fluence of $2.75 \cdot 10^{15} \text{ cm}^{-2}$. Solute transfer into the porous structure was confirmed by Secondary Ion Mass Spectrometry (SIMS) depth profiling of substrates after depositing 0.66 $\mu\text{g/g}$ aqueous solution of Eu (as a non-radioactive surrogate of Am) in 1 mol/L nitric acid onto etched and non-etched areas (see Supplement Figure 12).

2.7. DES

We use a dilution refrigerator with minimum base temperature $T_b \approx 20 \text{ mK}$, to enable continuous data acquisition over days to weeks. Higher T_b values up to 100 mK are reached by using a Proportional Integral Derivative (PID) controlled resistive heater on the cold flange (27 μK root mean square temperature stability). Radioactive decay energy is absorbed and converted into heat, seen as a temperature rise by a TES. Gold foil is used for the DES samples due to its favorable combination of stopping power and cryogenic thermal conductivity. The foil samples are thermally connected to the TES with gold wire bonds, gold ribbon bonds, or In-Ga eutectic (illustrated in Figure 2). The choice among these connection methods affects the pulse shape but does not substantially influence the resulting spectrum. The TES chip is thermally connected to the cold flange using gold wire bonds.

The TES is connected in parallel with a shunt resistor to provide a voltage bias. Current for TES bias is supplied by a room-temperature precision voltage source with a resistor divider. The TES current is amplified by a two-stage low noise Superconducting Quantum Interference Device (SQUID) amplifier (an input SQUID and a secondary SQUID array) maintained at a magnetic flux setpoint by a room-temperature feedback loop. The resulting analog signal (-10 V to 10 V) is sampled at 100 kHz with 16 bit ADC, and continuous data is stored on computer disc. Subsequently multiple triggering and analysis algorithms are applied to the stored data, to reduce the possibility of bias from a particular choice of algorithm.

In this study, three different types of TES chips were used (Table 1 and Figure 2), as they were modified to improve pulse shape uniformity and to reduce the number of flux jumps (see Section 5.3). The TES operates at

TES Chip	Metal Bilayer	Thermal Coupling	Cutout	Average Flux Jump Period	Chip Hit Proportion
CS04	Mo-Cu	Phonon weak link across etched structure	None	400 s	$\approx 3\%$
CS06	Mo-Au	Electron-phonon coupling in solid chip	None	8600 s	$\approx 0.5\%$
CS06C	Mo-Au	Electron-phonon coupling in solid chip	Silicon cutout under absorber	116000 s	$\approx 0.2\%$

Table 1: Three TES types used in this experiment, with average flux jump periods for Pass 1 ^{243}Am sources.

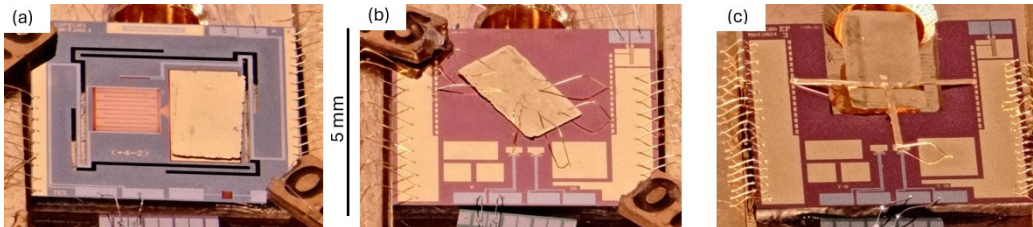


Figure 2: Photographs of TES chips used in this study, loaded with Pass 1 samples. (a) CS04 chip with absorber island and In-Ga eutectic sample attachment. (b) CS06 solid chip with wire bond sample attachment. (c) CS06C solid chip with silicon cutout under absorber with ribbon bond sample attachment (sample suspended by ribbon).

a temperature $T_c > T_b$, in our case $T_c \approx 100$ mK and T_b is set between 20 mK and 80 mK. An etched silicon meander structure is used to set the thermal coupling between T_c and T_b in the CS04 chip [42]. However the use of a meander causes the silicon of the absorber island to become part of the sensitive volume, so radiation absorbed by this silicon is observed as a fast pulse in the data stream. In the CS06 chip, the electron-phonon coupling between the TES and underlying silicon is used to set the thermal coupling strength, therefore radiation absorbed by the silicon has a relatively small impact on the TES signal (but not zero, see Section 5.2). Another practical advantage of the CS06 design is its mechanical robustness compared to the CS04 meander structure, making handling and sample exchange easier.

The CS06 design achieves an order of magnitude reduction in flux jumps from fast rising edge pulses. To further reduce direct radiation absorption in the TES chip, the cutout chip CS06C was designed, which minimizes the amount of silicon near the absorber. This achieves approximately another order of magnitude reduction in flux jumps (Table 1). This reduction improves confidence that biases are not introduced by the analysis method.

3. Pulse processing and data analysis

3.1. Pulse amplitude method

Analysis of stored continuous time stream data consisted of 3 steps: triggering pulses to produce pulse records, analyzing pulse records to produce live-timed energy spectra, and deriving nuclide activities from the spectra.

Pulse triggering was accomplished by convolving the voltage stream with a step filter, of length between 4 and 30 samples. A trigger threshold was applied to the output to trigger a pulse. A condition of multiple consecutive values above threshold applied to improve signal to noise. For each trigger, a pulse record was recorded consisting of approximately 300 digitized values before and after the trigger. Such a record would have length 6 ms and be centered on the start of the pulse. All triggered pulses were recorded, even if records were overlapping. The ^{243}Am sources were about 1.2 Bq, resulting in about $7.5 \cdot 10^4$ pulses recorded over a 24 hour run.

Pulse record analysis consisted of live-timing and pulse energy assignment. Live-timing [43] was accomplished by applying an extending dead time, set at 60 ms, chosen to be longer than any holdoff applied during triggering and long enough to avoid the most piled-up pulses. In addition, for each pulse, a condition was applied requiring no pulses within a fixed time after the trigger. This ‘forward dead time’ was typically set to be equal to the post-trigger duration of the pulse, to avoid pileup. If a subsequent pulse is found within this forward dead time, that dead time is extended to the next pulse. Thus, it was critical to avoid double-triggering, which if it occurred would cause excessive dead time. This condition was checked by examining the arrival-time distribution. The live-time method is illustrated in Figure 3 and Algorithm 1.

For each pulse record, the pre-trigger portion of the record was fit with a linear function. This fit was then extrapolated to and subtracted from the post-trigger portion of the record. For longer records with higher count rates, fitting an exponential function can improve energy resolution without the need of a long extending dead time. The pulse height was taken as the voltage at a set time delay after the trigger. This delay was set to about 1 ms (100 samples) to avoid sampling the start of a pulse (Section 5.2). The pulse amplitude was averaged over 15 samples. Pulse amplitudes were histogrammed and the energy scale calibrated using the ^{243}Am Q value for the full energy DES peak.

Algorithm 1: Live-timing with extending dead time

Data: Pulse trigger timestamps

τ_1 :=(regular) extending dead time;

τ_2 :=pileup time window or ‘forward dead time’;

for $i \leftarrow 1$ **to** *last pulse* **do**

$t_i \leftarrow$ time of pulse i ;

$dt_i \leftarrow t_i - t_{i-1}$;

if $dt_i > \tau_1$ **and** $dt_{i+1} > \tau_2$ **then**

 Process pulse energy;

$C_L \leftarrow C_L + 1$;

 // Increment live counts

$T_L \leftarrow T_L + dt_i - \tau_1$;

 // Increase live time

end

end

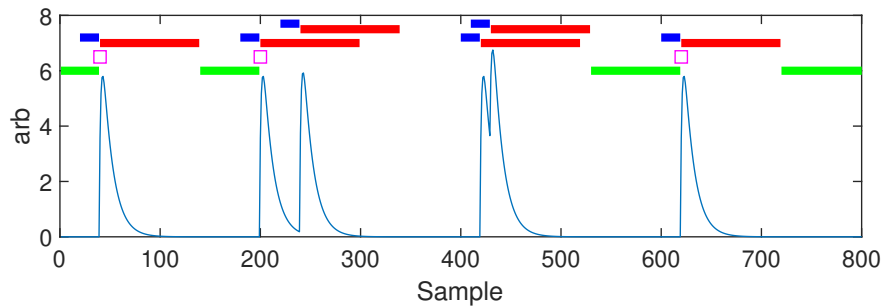


Figure 3: Illustration of live time algorithm with 3 live pulses (magenta squares), showing applied dead time after a pulse (red lines following each pulse), pileup time window (blue lines preceding each pulse), and live time region (green lines preceding live pulses). The pulse near sample 250 is excluded by dead time after a pulse, while both pulses near sample 430 are excluded by the pileup window, which also excludes the preceding live time.

3.2. Pulse integral method

The integral method is a physically motivated means to use all available pulses to generate a DES spectrum. Under a voltage bias, TES power $P = V \times I$ and V is constant (to first order). The recorded energy of a decay event may therefore be approximated by integrating the change in TES current from its baseline value over the duration of the decay pulse, from the start of the pulse to time t , $E(t) = \int_0^t P(\tau) d\tau = V \cdot \int_0^t (I_0 - I(\tau)) d\tau$. In the small signal limit and following the rising edge of the decay pulse, the TES current is observed to return to its baseline value in a decaying exponential manner, $I_0 - I(t) = C \cdot e^{-bt}$ (C is current amplitude, b is decay constant, C, b, t positive). Thus for a decay pulse with instantaneous rising edge at $t = 0$ to amplitude C , using Eq. 4, $E(\infty) = V \cdot C/b$.

$$\int_0^{\infty} C \cdot e^{-bt} dt = C/b \quad (4)$$

With a pulse represented by Equation 4, the integral will include 99.9% of the total pulse energy at $t \approx 6.9/b$ or 40 ms for our TES detectors. Pileup within this integration period will cause a significant sum peak fraction in the spectrum. Therefore an approach has been developed to apply pileup correction to pulse integral values (Figure 4).

First, a digital filter is applied to the data stream to locate the rising edge of each pulse. The filter needs to accurately identify pulses that are on the falling edge of a previous pulse, and to avoid double-triggering on irregular shape pulses. There are numerous filters that can satisfy these requirements, such as step and trapezoidal; we have found slightly improved performance with an overlapping second-derivative filter tuned for orthogonality to the exponential decay of the falling edge. Second, pulses are categorized as piled-up or not piled-up based on the proximity of their rising edges to previous pulses and known b . Signal baseline is measured in pulse-free regions. Third, the piled-up pulses are compared to non piled-up pulses to build an empirical model of the normalized pulse integral function (Eq. 5) where $M(t)$ is the normalized integral value at time t from pulse start, C_i and b_i are tuned to match observed pulses, and N_e is chosen as low as practical (typically 1 or 2) to match the TES detector response. Note this model function could be arbitrarily defined, as long as it matches the observed pulse characteristics; for our detectors a sum of decaying exponentials gave a satisfactory fit. Fourth, the model function along with known t and partial integral $E(t)$ at

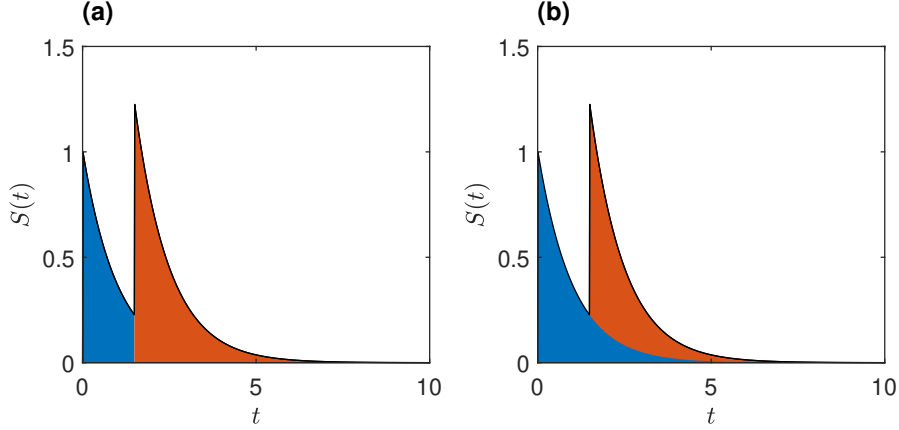


Figure 4: Integral correction method with two simulated instantaneous rising edge pulses, each described by Eq. 4 with $C = 1, b = 1$. (a) The signal over time is integrated, shown by the blue and orange areas under the curve. Based on pulse rising edge time, the blue area is assigned to pulse 1, and orange area is assigned to pulse 2. (b) The same signal with pileup correction, with the blue area extrapolated using Eq. 5 and subtracted from the second pulse.

the observed point is used to correct the energy of piled-up pulses (Eq. 6), by adding energy to pulses that cannot be integrated fully, and subtracting energy from future pulses that are on the tail of a given pulse (illustrated in Fig. 4(b)).

$$M(t) = 1 - \sum_{i=0}^{N_e} C_i \cdot e^{-b_i \cdot t} \quad (5)$$

$$E(\infty) = \frac{E(t)}{M(t)} \quad (6)$$

In this manner all pulses contribute to the spectrum, with pulses that are cut short by pileup requiring a higher amount of correction by the model, while pulses that are not piled-up are integrated with minimal correction. Since $M(t)$ only acts as a correction for moving energy between pulse assignments, it does not affect the total energy balance or the number of pulses counted. The function will only generate a clean spectrum if it is a good match to pulse characteristics, hence the choice of (C_i, b_i) is not arbitrary. With a stable baseline, it is possible to track energy balance during the entire acquisition period, which increases confidence for metrology results. After

generating a corrected pulse energy spectrum, the analysis methods for massic activity determination are the same as for pulse amplitude.

3.3. Massic activity

Deriving radionuclide activities from the processed spectrum was accomplished by region of interest (ROI) analysis, aided by Monte Carlo simulations (Section 3.4). As preliminary examination of the spectrum indicated that the alpha region was $> 99\%$ ^{243}Am , the activity, A , of ^{243}Am was derived from the total count rate within the alpha ROI, corrected for background, impurities, and decay.

$$A = \left(\frac{N_{\text{ROI}}}{t_{\text{L}}} - B_{\text{ROI}} \right) \cdot \left(1 + \sum f_{\text{imp}} \right)^{-1} \cdot D, \quad (7)$$

where N_{ROI} is the number of counts in the ROI, t_{L} is the live time, f_{imp} is the ratio of impurity radionuclides to the main nuclide, B_{ROI} is the background count rate in the ROI, and D is the decay correction to a reference time.

The massic activity for a source of mass m is given by

$$C_A = \frac{A}{m} \cdot \frac{1}{1 - L}, \quad (8)$$

where L is the fraction of activity, if any, dispensed onto a foil that ends up on the placemat, typically $< 0.2\%$, determined from the relative LS count rate for the placemat (R_{PM}), the number of drops dispensed onto the corresponding foil or foils sitting on the placemat (N_{foil}), and the LS count rate ($R_{\text{LS-i}}$) for N_{vial} drops dispensed directly into a vial. This method does not rely on knowing the LS counting efficiency, only that it be the same for gels and pure LS sources. A previous study, [44], found no systematic difference in LS efficiency for ^{241}Am and a 2% relative uncertainty in LS efficiency for the two types of sources.

$$L = \frac{R_{\text{PM}}/N_{\text{foil}}}{R_{\text{LS-i}}/N_{\text{vial}}} \quad (9)$$

3.4. Monte Carlo simulations

Determination of nuclide activities other than the main nuclide is accomplished with the aid of a Monte Carlo model to estimate the contributions of ^{243}Am , if any, in the ROI of the other nuclides. Pioneering DES measurements of $^{240}\text{Pu}/^{239}\text{Pu}$ isotopic ratios referred to the method as ‘Q spectroscopy’ since, for these radionuclides, the resulting DES spectrum was a

single peak per nuclide at the Q value (total transition energy) [29]. Those nuclides decay to low-energy states that subsequently de-excite primarily by conversion electrons, Auger electrons and x-rays, which are absorbed in the gold absorber, summing with the alpha particle and recoil nucleus energy well within the resolving time of the detectors. The resulting DES data could be well fitted using a single peak per nuclide, described by typical Bortels functions, consisting of a Gaussian and multiple exponential tails [45].

However, in the case of ^{243}Am , the decay includes branches through high-energy daughter states that decay by significant probability through higher-energy γ -rays up to 195 keV, with a significant branch at 75 keV (67 %). These gamma-rays can escape the absorber foil, leading to escape events either directly, as escape peaks, or after Compton scattering. Additional energy can escape from deexcitation x-rays or x-ray fluorescence of the gold. For ^{239}Np , the beta particles themselves can also escape the foil, as can bremsstrahlung. Thus, for the present work, a Monte Carlo simulation of the source-detector system was developed. The model would be used to account for the various features of the spectra, predict spectral signatures for observed or potential impurities, and fit the spectrum to disentangle interfering radionuclides in the DES.

The detector chips and absorbers were modeled using Geant4 [46]. The model was run for all potential radionuclides in the sample, for a variety of foil thicknesses. Then the experimental spectrum was fit using a linear combination of the simulated spectra with the activity of each nuclide, energy resolution, left and right tail parameters as free parameters. Since the foil thicknesses are not uniform after rolling, a distribution of thicknesses was allowed in the model, implemented as a linear combination of two or three thicknesses. Additionally, for impurity nuclides with Q values above and close to the main nuclide, pileup was simulated to account for small amounts of pileup in the spectrum caused by missed triggers, especially when a sample contains both alpha and beta decay (such as ^{243}Am with ^{239}Np).

The fitted spectrum served multiple purposes. First it confirmed that all spectral features are accounted for, thus enabling search for unexpected impurities. Second, where spectral overlap occurs, it was used to estimate the tailing of one nuclide from under the ROI of another. Finally, the model was used to carry out sensitivity tests for estimating uncertainties due to pileup and to put upper limits on non-detected potential impurities.

The model was built on version 4.10.7.2 of the Geant4 toolkit [46]. The geometry consisted of a rectangular gold absorber set to twice the thickness

of the gold foil (since the foil is folded in half before measuring). The activity was distributed uniformly in a volume 1 mm by 1 mm by 1 μm centered in the absorber. The absorber foil sat atop a silicon rectangular solid representing the chip of thickness 275 μm and side length 4.5 mm.

Within Geant4, radioactive decay and electromagnetic physics were implemented via the `BiasedRDPhysics` and `G4EmStandardPhysics_option4` classes, respectively. Within the absorber, a photon and electron cut value of 1 μm was used. The model was run for at least $1 \cdot 10^6$ histories for a given geometry. The total energy deposited in the foil, in the chip, and combined, were tallied in histograms. Optionally, Gaussian and exponential tail noise could be added in the simulation. But for the present work, that option was not used as noise was added later during spectrum fitting. Random summing spectra were also simulated for ^{243}Am and ^{239}Np with each other and themselves. Previous work on ^{241}Am , without impurities, indicated that the model could fit experimental spectra adequately for the purpose [15].

For this work, a spectrum fitting program was created, using the output of the Geant4 model. Since the source geometry was not perfectly known (e.g., hand-folded foils, uncertain dried deposit geometry, thinned edges during rolling), each spectrum was fit with a linear combination of spectra having thicknesses that bracket the true expected mean thickness. Additional free parameters were nuclide ratios (^{243}Am , ^{239}Pu , ^{239}Np , ^{241}Am), gaussian noise, exponential tail parameters (two low energy tails, one high energy tail), and random summing ratio. These parameters were adjusted manually or automatically to maximize goodness of fit. The fits were examined for any unexplained features, and the ^{243}Am component of the fit was subtracted from the ^{239}Pu region of interest and the random summing of ^{239}Np and ^{243}Am was subtracted from the ^{241}Am region.

4. Results

4.1. Mass of dispensed solution

The mass of solution deposited to each TES foil was determined by both method 1 and method 2 (defined in Section 2.3).

For method 1, the inkjet mean drop size was calibrated by the ultramicrobalance 7 times during the source preparation session: once before the first pass, twice between the first and second passes, and four times after the second pass (Figure 5). The average drop mass increased by about 0.28 % over a period of one hour. It was not expected that the drop mass dispensed

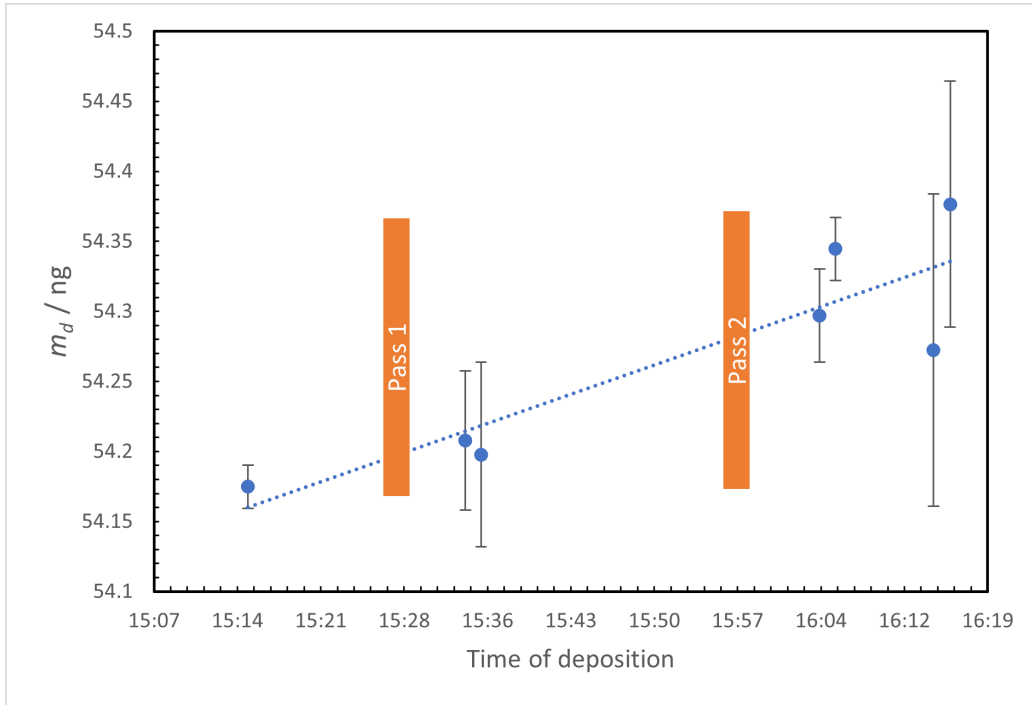


Figure 5: Method 1 drop mass (m_d) calibrations during inkjet deposition, linear fit used to determine m_d for Pass 1 and Pass 2 depositions.

by inkjet would remain constant during the entire experiment. As drops are ejected, evaporation and other changes around the device orifice subtly change surface wettability and hence the drop formation dynamics. A linear fit of drop mass vs. time was used to interpolate the drop mass during the deposition of the first pass and second pass.

The Riserate and Burst values of average drop mass were within 0.2% of each other. We accepted the average value for two variations of the Riserate procedure and two variations of the Burst procedures (defined in Section 2.3). Figure 5 shows the standard uncertainty for the drop masses determined in this manner. A correction for mass loss between ejection and impact with the fluid in the weighing vessel was based on a prior experiment where drop masses were determined across four weighing vessels having different levels of fluid, hence changing the flight distance. It was found that keeping the fluid level high and flight distance at about 3 mm would limit drop mass loss to about 0.1%. A buoyancy correction of $(0.11 \pm 0.01)\%$ was also applied [47].

	Method 1		Method 2			Adopted	
Pass	$m / \mu\text{g}$	$u / \mu\text{g}$	$m / \mu\text{g}$	$u / \mu\text{g}$	D/u_D	$m / \mu\text{g}$	$u / \mu\text{g}$
1	61.91	0.12	61.65	0.11	-1.61	61.78	0.22
2	62.00	0.12	61.89	0.11	-0.69	61.95	0.14

Table 2: Results for TES source masses, $m = m_d \cdot N_{\text{foil}}$, and uncertainties by calibration method 1 (inkjet balance) and method 2 (pycnometer + LS ratio). The difference, D , between methods divided by its uncertainty. The adopted value is the average of the two methods.

For method 2, the LS sources prepared by pycnometer before and after the inkjet experiment, those prepared by inkjet deposition, and the blank, were measured in the two LS counters. For the mass calibration, only the data from the Tricarb were used, since the wide energy window and lack of pulse shape discrimination were expected to give the most consistent efficiency among samples.

To check for activity concentration changes during the experiment, the mean massic LS rate for the pycnometer-prepared sources from before and after the inkjetting were compared. The change was $(0.06 \pm 0.08)\%$, indicating that there was no significant change in concentration, where the uncertainty is from the standard deviation of the replicate sources.

The results for average masses of solution deposited onto the TES foils for both method 1 and method 2 are shown in Table 2. The uncertainty budget for method 1 is shown in Table 3, where the largest source of uncertainty was the uncertainty on the regression fit, which includes contributions from measurement repeatability. The uncertainty budget for method 2 is shown in Table 4, where the largest source of uncertainty was the balance calibration for the 7 mg solution masses determined by pycnometer weighings. Both linearity and offset uncertainties were considered.

For the final massic activity, the mass of each TES source was taken to be the average of the values from method 1 and method 2, with the uncertainty taken as the standard deviation of the average masses by the two methods, combined in quadrature with the average uncertainty of each method.

4.2. Placemat results

The LS sources containing the gel placemats, one containing a blank gel, and two blanks containing the LS cocktail without gels were counted for 300 minutes in both LS counters. As the Quantulus counter had $10\times$ lower

Item	$u_i / \%$	A or B	Description
Dynamic use of microbalance	0.10	B	includes linearity
Buoyancy correction	0.01	B	correction of 0.11 %
Evaporation-in-flight	0.05	B	correction of 0.10 %
Algorithm coverage	0.065	A	SD of 4 algorithms
Regression	0.16	A	includes repeatability
u_c	0.21		

Table 3: Uncertainty budget for mass of solution dispensed onto each TES foil, determined by method 1. Dynamic use of microbalance is described elsewhere [48]. Linearity uncertainty was (0.9 μg across 2.1 g range) as stated in balance manual.

Item	$u_i / \%$	Type	Description
repeatability	0.01	A	average SD of replicate LS sources
potential evaporation	0.04	A	SD of average massic LS rate before and after inkjet
balance calibration	0.15	B	linearity and offset specifications
LS precision	0.08	A	SD of 3 repeat measurements on each source and 1 blank
drop consistency	0.03	A	SD of 3 LS sources bracketing each TES pass
blank	0.01	A	SD of long measurements on 2 blanks
u_c	0.18		

Table 4: Uncertainty budget for mass of solution dispensed onto each TES source using method 2, where SD is standard deviation.

background in alpha-beta discrimination mode (set for alpha), it was used for the placemat analysis. There was no statistical difference in the count rates among the three blanks. The blank rate was taken as the average of the three with the uncertainty being the average Poisson counting uncertainty among them, to represent the uncertainty in the blank count rate for any given source. The average blank count rate was $(0.075 \pm 0.004) \text{ s}^{-1}$ (the standard deviation of the distribution was 0.002 s^{-1}). With this low background, a small, potentially significant activity was found on two of the placemats. The fraction, L , of dispensed activity that was lost to the gel, for the three gels was $(0.11 \pm 0.06) \%$, $(-0.03 \pm 0.10) \%$, and $(0.01 \pm 0.03) \%$, where the uncertainties are from Poisson counting statistics for the source and blank measurements.

These values were used in the massic activity calculations by Equation 8.

4.3. Activity results

Three ^{243}Am sources and a blank from Pass 1 and three ^{243}Am sources from Pass 2 were measured on one or two occasions for about 24 hours per run. Example decay energy spectra for various combinations of source and detector type are shown in Figure 6. For the active sources, the total trigger rate was about 2.6 s^{-1} and with the extending dead time and pileup time window (see Section 3.1) set to 60 ms and 5 ms, respectively, the live time fraction was about 0.85.

For Pass 1 substrates, there is some low energy tailing, or ‘grass’ in the spectra (6a), below the alpha region. This amounts to between 0.3% and 1.0% of the alpha counts, depending on the source. These counts are attributed to the fact that Pass 1 foils were smaller than Pass 2 with the top side covered with a hydrophilic npAu coating, such that the solution had filled the surface of the foil all the way to some edges. After the foil was folded and rolled, the edges of the foil were visibly thinner than the central regions. Thus, some alpha particles penetrated the foil after depositing only some of their energy.

In contrast, the Pass 2 substrates were larger gold foils with a hydrophobic coating that had been deposited over the top side of the foil. A smaller rectangle in the center of each source was etched away with a laser. This etching was only partially effective, as evidenced by beading up of the solution that was observed during deposition. In the spectra (6b), the lack of grass is interpreted as an indication that the hydrophobic coating was successful in keeping the activity away from the edges of the source. However, the ‘wings’ on the alpha peaks could be an indication of chemical effects due to incomplete removal of the hydrophobic coating in the center of the source. For the ^{239}Np spectra from Pass 2, high energy tailing is visible in the CS06 chip but not the CS06C (cutout) chip. This may be attributable to beta particles escaping the foil and hitting the chip, as discussed further in Section 5.2.

Despite the various non-ideal spectral features, spectra for all 6 ^{243}Am sources and the blank were adequate for determining the total α -decay rate and to search for radionuclide impurities. Results from 4 sources were adequate for determining ^{241}Am impurity fraction, and 3 sources for the ^{239}Pu impurity fraction. Further, the ^{239}Np spectra were observed in all sources and analyzed for approximate activity.

The blank was measured on multiple occasions for at least 24 hours. An approximate energy calibration was performed using the 122 keV line of a ^{57}Co source placed outside the cryostat. Nonlinearities in the energy calibration of about 1% between 122 keV and 5.4 MeV are expected based on ^{57}Co irradiation of ^{243}Am samples, but were not accounted for here since the background was insignificant for the measurands of this work. For a 65 hour measurement, the average background rate was $(2.87 \pm 0.11) \cdot 10^{-3} \text{ s}^{-1}$ and the total number of counts with energy above 1 MeV was zero (Figure 6).

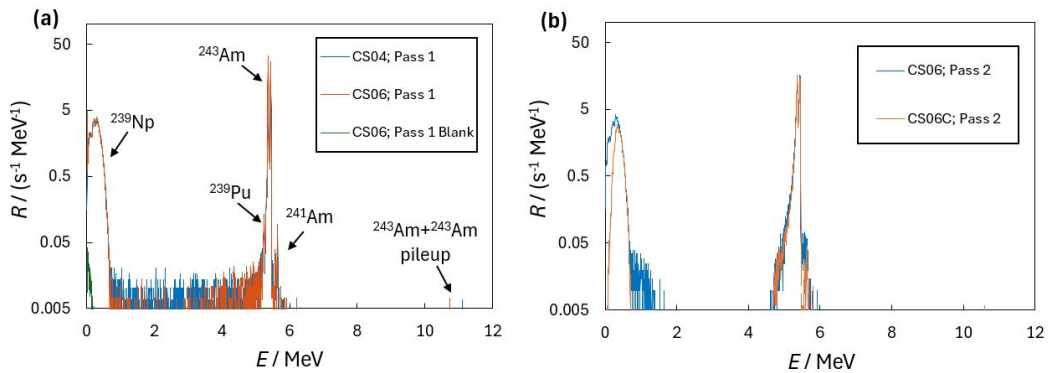


Figure 6: Spectra from four ^{243}Am sources and one blank. a) Pass 1 sources reveal the presence of ^{241}Am and ^{239}Pu and some ‘grass’ between 1 MeV and 4.5 MeV. b) For Pass 2 sources, the grass is not present, though ‘wings’ are visible on the alpha peaks and for CS06 detector, some ^{239}Np chip hits above the endpoint energy. See text for details and Fig. 7 for spectral analysis.

Spectra were overlaid with Monte Carlo simulations to ensure that all spectral features were adequately accounted for by the radionuclides that had been identified. Figure 7 shows an example spectrum with simulation. The best fit was obtained using a combination of simulated Au foil thicknesses (10 μm and 20 μm), consistent with the hypothesis that the edges of the foil were rolled thinner than the center. For ^{239}Np , the simulation qualitatively matches the experimental spectrum (Figure 7a). The summing of the energy of beta particles with atomic cascade radiation and gamma de-excitation energy, in particular conversion electrons, along with the escape of a substantial part of the gamma-rays from the absorber, explain the structures observed in the ^{239}Np region. The few counts above the β -particle endpoint were simulated as pileup, though an exact simulation of pileup is tricky due to the fact that it is only in the case that the trigger filter misses a pulse that it would appear in the spectrum. Without further characterization of detection

efficiency for low-energy decays, full activity determination for ^{239}Np was not attempted. For the two sources with the lowest noise floor, the ratio of the net ^{239}Np to ^{243}Am count rate was 0.982 ± 0.005 and 1.000 ± 0.005 . The lower threshold was about 11 keV, which in the simulation corresponded to 99.5% of the ^{239}Np spectrum.

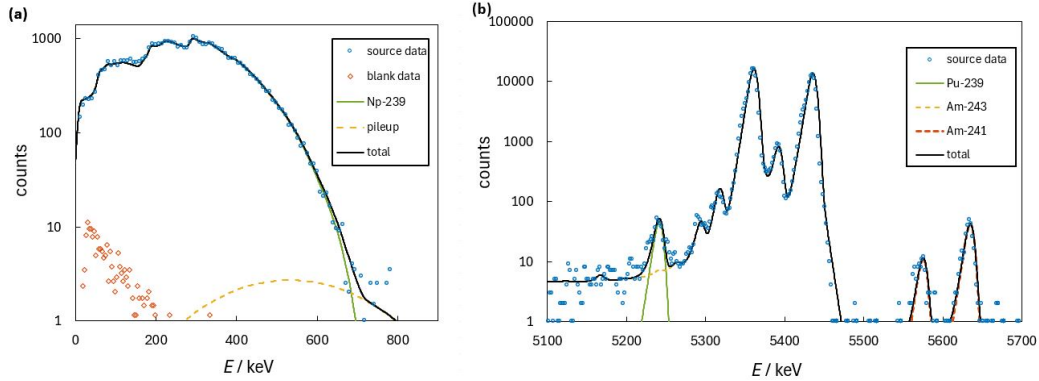


Figure 7: DES spectra with Geant4 Monte Carlo simulations. a) ^{239}Np region features significant summing of β -particles with secondary radiation (see text). b) α -decay ROI counts are explained by presence of ^{239}Pu and ^{241}Am in the sample. For ^{239}Pu quantification, the simulation fit for ^{243}Am was used as an alternative to the average count rate on each side of the peak.

For the α -decay analysis, Equation 7 was used. The ROI was set from the end of the β -region to the end of the spectrum, including the ^{243}Am - ^{243}Am sum peak, which accounted for about 0.03% of events. To determine the ^{241}Am and $^{239,240}\text{Pu}$ content, two methods were used to set the background to subtract under the respective ROIs. One method was to extrapolate a linear function below the ROIs and the other was to use the simulation for ^{243}Am , the latter shown by the yellow dashed line under the $^{239,240}\text{Pu}$ peak in Figure 7b. For ^{241}Am , interferences, when present, were from pileup of ^{243}Am with non-triggered ^{239}Np pulses. These were simulated, when needed, or significantly reduced by applying pulse-shape discrimination (see Sec. 5.4).

Results for massic activity measurements are shown in Table 5, including ^{241}Am results for six samples using Equation 8. Impurity results were calculated for a subset of samples, having adequate spectral features (generally, low enough peak tailing). For the other samples, the impurity correction (Equation 7) was made using the average f_{imp} . As shown in Table 5, the massic activity of the six sources agree within statistical uncertainties. No

Pass	Chip	$C_{243\text{Am}} / (\text{kBq/g})$	$f_{241\text{Am}} / \%$	$f_{239\text{Pu}} / \%$
1 (2B)	CS06	19.23 ± 0.06	0.153 ± 0.013	0.166 ± 0.013
1 (1B)	CS04	19.29 ± 0.06	0.149 ± 0.011	0.165 ± 0.012
1 (3C)	CS06C	19.34 ± 0.08	0.166 ± 0.046	0.120 ± 0.026
2 (2A)	CS06C	19.31 ± 0.06	0.162 ± 0.013	—
2 (2C)	CS06C	19.28 ± 0.07	—	—
2 (3A)	CS06	19.31 ± 0.06	—	—
Average		19.293 ± 0.036	0.158 ± 0.008	0.150 ± 0.026

Table 5: Results for DES measurements on 6 samples by pass type and TES chip type. Massic activity results for ^{243}Am and impurity ratios ($f_{\text{imp}}=f_{241\text{Am}}$ or $f_{239\text{Pu}}$) are shown with statistical uncertainties only, due to Poisson counting in each ROI and extrapolation under peaks. Measurements for which spectra were not adequate for extracting impurities have no impurity results shown and use the average of the results for the other methods to make the small correction for ^{243}Am . The averages are unweighted. The uncertainty listed for the average is the standard deviation of the distribution among sources, showing agreement with the statistical uncertainty for each source.

significant difference between Pass 1 and Pass 2 sources is seen. A full uncertainty budget for the ^{241}Am massic activity is given in Table 6. The final result is $C_A = (19.29 \pm 0.07) \text{ kBq/g}$, where the largest sources of uncertainty were the sample-to-sample variability and mass determination.

In the SRM based on the same stock solution as measured here [21], a dilution factor of 398.29 ± 0.08 was applied, which corresponds to a DES-determined massic activity of $(48.44 \pm 0.19) \text{ Bq/g}$. The LS-based certificate value was $(48.42 \pm 0.12) \text{ Bq/g}$, with the DES value higher by $(0.02 \pm 0.22) \text{ Bq/g}$ ($z = 0.09$).

The final DES impurity ratios were $f_{241\text{Am}} = (1.58 \pm 0.08) \cdot 10^{-3}$ and $f_{239\text{Pu}} = (1.50 \pm 0.19) \cdot 10^{-3}$, where the standard uncertainties combine counting statistics, spectral analysis (varying ROI, agreement with Geant4 simulation) and between-source variability. The SRM impurity ratios using mass spectrometry were $f_{241\text{Am}} = (1.601 \pm 0.010) \cdot 10^{-3}$ and $f_{239\text{Pu}} = (1.248 \pm 0.005) \cdot 10^{-3}$. The differences between DES and mass spectrometry values divided by their combined uncertainties are $z = -0.26$ and $z = 1.3$, for $f_{241\text{Am}}$ and $f_{239\text{Pu}}$, respectively.

Item	$u_i/\%$	Type	Description
Reproducibility	0.19	A	From Table 5
Mass	0.30	B	Average from Table 2
Background	0.001	B	Assume 1 count (0 counts observed)
Alpha ROI	0.1	B	From correction for alpha counts in beta region (correction was 0.00 % to 0.17 %)
Pu-239 impurity	0.02	A	From Table 5
Am-241 impurity	0.008	A	From Table 5
Live time	0.1	B	Parameter variation and comparison between amplitude and integral methods
Half-life	$3 \cdot 10^{-5}$	B	From DDEP half-life
u_c	0.38		

Table 6: Uncertainty budget for ^{243}Am massic activity, C_A .

5. Discussion

5.1. Sample preparation

The Pass 1 samples were made on smaller foils which improved pulse amplitude due to lower heat capacity, however there was a higher prevalence of chip hits compared to Pass 2. This suggests that during the deposition process, some of the solution dried near the edges of the foil, and the subsequent rolling did not encapsulate that portion of the source within the expected gold thickness. This may be due to a combination of solution wicking through the nanoporous layer which extends to the edges of the foil, small indentations in the foil after laser etching and cutting (pinholes were ruled out by optical microscopy prior to deposition), and thinning out of foil edges due to the rolling process. Multiple groups report that kneading and mechanical working of the absorber helps improve energy resolution [29, 23, 30], which was not done in our case to ensure that all deposited activity remained inside the absorber (instead nanoporous gold is used [28]).

5.2. Pulse shape variability

Different pulse shapes are commonly encountered due to variations in heat flow after the decay event. Radiation that is not fully absorbed by the absorber (in particular gamma and beta) can interact with the TES chip as ‘chip hits’, causing localized heating and a changed pulse since the heat flow bypasses the thermal mass of the absorber (Fig. 8). This may generate a

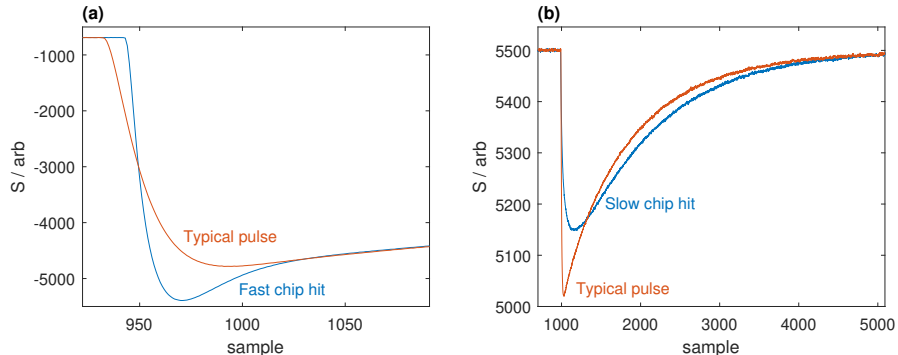


Figure 8: Representative pulse shapes showing chip hits in two TES chip designs. (a) The CS04 absorber island absorbs the particle energy, causing a fast rising edge. (b) The CS06 does not have an absorber island, so the particle energy causes a slow falling edge.

continuum of shapes, depending on the fraction of energy deposited into the TES and into the absorber. While our absorber thickness is chosen to stop alpha particles, it is not expected to fully stop beta or gamma radiation. The presence of chip hits is addressed in our case by reducing the mechanical cross-section of the TES and silicon chip as seen from the absorber, and by strongly heat-sinking the chip to the sample box.

Other causes of pulse shape variability were also considered, but were not of significance in this measurement. Radiation may generate quasi-particles or long-lived states that lengthen the pulse [49]. This is avoided in our case by using a gold (normal conducting) absorber and using only metallic elements (rather than epoxy) for absorber attachment, resulting in a highly exponential pulse falling edge.

After deposition and drying, radioactive atoms are distributed at different locations in the absorber, which causes differences in thermal path lengths to the TES. When this effect is controlled it may be used for position imaging [50, 51]. It is possible that our spectrum peaks are broadened by this effect, due to the relatively large absorber dimensions.

Decay events occur at random phase relative to the Analog Digital Converter (ADC) sample clock. This may be addressed by scanning the filter envelope with sub-sample time offsets and picking the best fit. For pulse amplitude analysis, a flat region of the pulse peak was used which reduced sensitivity to this effect, confirmed by varying analysis parameters.

When the TES is biased near an unstable region of electro-thermal feed-

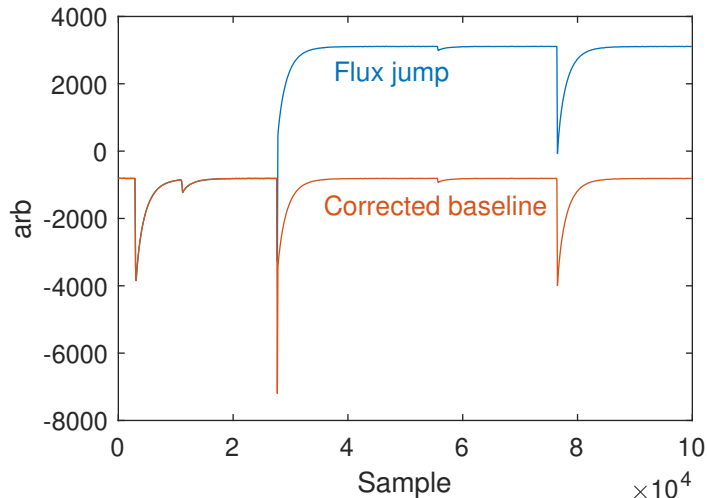


Figure 9: Example digitized data showing a flux jump after a fast pulse rising edge, and offline correction of the flux jump by restoring the baseline (a few samples on the rising edge cannot be corrected unambiguously).

back [52], ringing may be observed following the rising edge of the pulse. The ringing is typically consistent but has high sensitivity to changes in T_b or bias current. For pulse amplitude analysis, the pulse amplitude is averaged after the ringing has decayed. It is important to avoid multiple-triggering from the multiple rising edges of the ringing waveform, especially if this introduces dead time or double-counting. When ringing was observed, the trigger filter threshold and holdoff time were chosen to ensure a single trigger per pulse.

5.3. Flux jumps

The signal passes through a two-stage SQUID amplifier which uses a feedback loop to maintain a preset magnetic flux through the SQUID sensing coil. A pulse with a fast rising edge in excess of the feedback loop maximum slew rate causes a jump in the amplified signal by a multiple of the current corresponding to a magnetic flux quantum (Figure 9).

ADC saturation due to flux jumps is avoided by using sufficient dynamic range in the electronics to allow for a few flux jumps without clipping, and re-setting the feedback loop to a 0 V signal level before the ADC is saturated.

A more critical challenge of flux jumps is that they are always caused by the fast rising edge of real decay events (for a properly tuned system),

therefore excluding them from analysis will incur some bias on the result. It is preferable to reduce the incidence of flux jumps by improving sample preparation and TES chip design, as discussed in Section 2.7.

5.4. Pileup pulses

All current-generation cryogenic detectors used for DES have a slower response time (1 ms to 10 ms) than typical room-temperature radiation detectors. This constrains the activity that can be enclosed in DES absorbers to approximately 10 Bq. Source activity lower than this complicates the gravimetric link to typically used source solutions (requiring a dilution or a reduced number of inkjet drops), and increases counting time. When absolute activity is the goal, exclusion of pileup pulses impacts counting statistics and may introduce errors such as complete removal of short (1 ms to 10 ms) half-life nuclides or their parent from the spectrum.

The presence of pileup pulses is greatly reduced using extending dead time and pileup time window rejection with live-timing, as the only pulses that are analyzed for energy are those with no other pulse, before or after it within a set time window, chosen to be longer than the portion of the pulse used for energy determination. For quantifying the ^{241}Am impurity in a sample containing ^{243}Am in equilibrium with ^{239}Np , further pileup rejection is desirable since the ^{241}Am region of the spectrum is within the summing range of the other two nuclides, both of which are decaying with about the same rate. An approach was implemented in which pulses falling within the ^{241}Am ROI were analyzed for pulse shape, by residual standard deviation (RSD) from the mean pulse shape, to remove pileup pulses that did not trigger due to a small ^{239}Np pulse being missed by the trigger algorithm. This method is susceptible to biases since the pulse-shape analysis could catch chip hits or other pulse shapes that are true ^{241}Am pulses. This risk was mitigated by limiting the RSD to the region after the peak (samples 400 to 600, Figure 10). Spectra were analyzed with and without the RSD cut (Figure 10).

6. Conclusion

The DES massic activity result has comparable uncertainty to traditional, non-spectroscopic methods such as liquid-scintillation counting. In the past the ^{239}Pu and ^{241}Am activity was not included in the ^{243}Am SRM. LS counting and alpha spectrometry are sensitive to contributions from these impu-

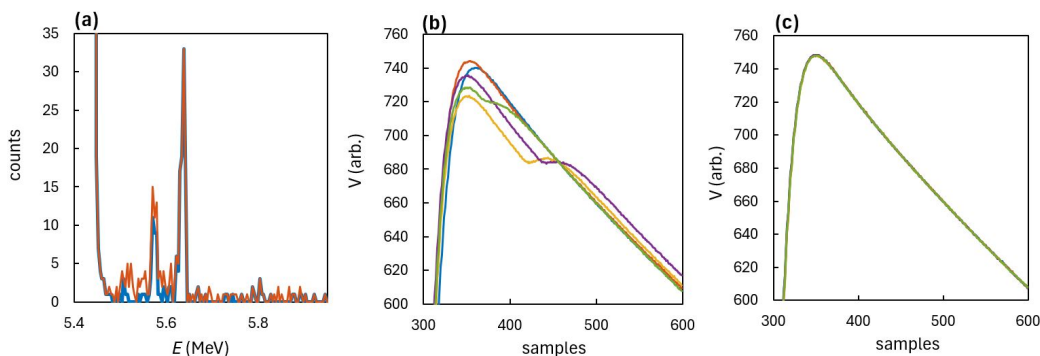


Figure 10: Example of RSD cut. (a) Shows ^{241}Am region of DES spectrum (Q peak and escape peak) to the right of the ^{243}Am region with before (orange) and after (blue) the RSD cut, which reduces the $^{243}\text{Am} + ^{239}\text{Np}$ pileup continuum by a factor of about 2.5. (b) Five pulses cut by RSD filter and (c) five pulses not cut are shown. The energy filter averaged over samples from 450 to 465. No pileup events after that range appear since those events would not be above the ^{243}Am ROI.

rities, and quantifying them would include additional correction of tracer impurities and mass spectrometry isobaric interferences. DES offers an intrinsic treatment of such impurities by quantifying multiple radionuclides, of multiple atomic species, at once without the need for chemical separation, tracers, or efficiency calibrants.

For massic activity, two methods have been demonstrated for determining mass of solution at the much smaller (microgram) mass level needed for the DES samples. Method 1 uses direct calibration of the mass of a drop of solution from the inkjet and is widely applicable, while Method 2 uses relative LS measurements to link to pycnometer measurements and can provide lower uncertainties for select experiments (when adequate LS rates and reproducibility are achievable) without requiring an integrated microbalance as part of the inkjet system. In this work, estimated mass uncertainties of 0.30% were achieved. The dominant uncertainties for DES differ from other methods, making it a valuable metrology tool.

7. Acknowledgments

This work was supported in part by National Institute of Standards and Technology IMS funding.

Certain commercial equipment, instruments, or materials are identified in this paper to foster understanding. Such identification does not imply

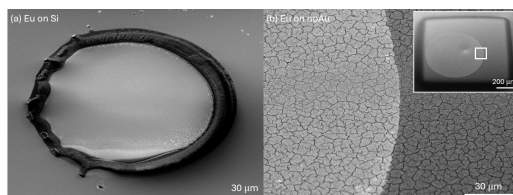


Figure 11: Scanning electron micrographs showing the deposit morphologies of EuCl_3 in 1 mol/L HNO_3 solution on (a) non-porous silicon wafer ('coffee ring' visible) and (b) nanoporous Au layer. The concentration was $0.66 \mu\text{g/g}$ of solution, and the deposited amount was 0.028 ng (500 drops of 86 ng solution) using a drop-on-demand deposition printer. Clear differences are shown with respect to the spatial distribution of material on the surface. In (b), the inset shows the less magnified area of the dried deposit, which was deposited inside a 1 mm square area where the hydrophobic layer was etched away using an energetic ion beam.

recommendation by the National Institute of Standards and Technology, nor does it imply that the materials or equipment identified are necessarily the best available for the purpose.

8. Supplement

References

- [1] C. Michotte, L. Johansson, CCRI (II) activity comparison of ^{241}Pu : CCRI (II)-K2. Pu-241, *Metrologia* 49 (1A) (2012) 06012–06012.
- [2] M. Loidl, M. Rodrigues, B. Censier, S. Kowalski, X. Mougeot, P. Cassette, T. Branger, D. Lacour, First measurement of the beta spectrum of ^{241}Pu with a cryogenic detector, *APPLIED RADIATION AND ISOTOPES* 68 (7-8) (2010) 1454–1458, 17th International Conference on Radionuclide Metrology and Its Applications (ICRM 2009), Slovak Inst Metrol, Bratislava, SLOVAKIA, SEP 07-11, 2009. doi:10.1016/j.apradiso.2009.11.054.
- [3] L. C. Angrave, N. E. Booth, R. J. Gaitskell, G. L. Salmon, M. R. Harston, Measurement of the atomic exchange effect in nuclear β decay, *Phys. Rev. Lett.* 80 (1998) 1610–1613. doi:10.1103/PhysRevLett.80.1610. URL <https://link.aps.org/doi/10.1103/PhysRevLett.80.1610>

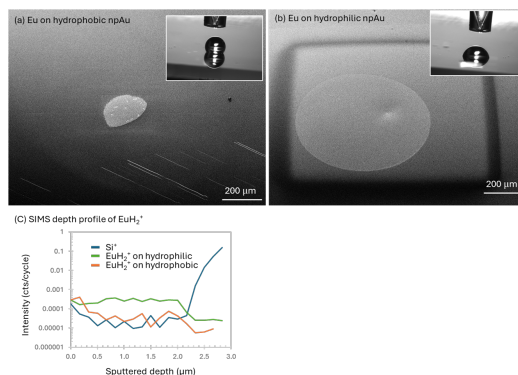


Figure 12: Scanning electron micrographs showing the deposit morphologies of EuCl_3 in 1 mol/L HNO_3 solution on (a) hydrophobic npAu and (b) hydrophilic layer. The insets show photographs of droplets in contact with the surface. The contact angles were 127° and 79° , respectively, which resulted in differently sized footprints. The deposited amount of EuCl_3 per spot was 0.028 ng. (c) SIMS depth profiling of the EuH_2^+ ions as a tracer shows the extent of volumetric transfer through the two solids, with the hydrophobic layer showing a majority of the signal closer to the surface and the hydrophilic layer showing uniform distribution throughout the film. The main finding here is that the solution was able to wick into the hydrophilic film after etching of the hydrophobic layer.

- [4] X. Mougeot, C. Bisch, Consistent calculation of the screening and exchange effects in allowed β^- transitions, *PHYSICAL REVIEW A* 90 (1) (JUL 2 2014). doi:10.1103/PhysRevA.90.012501.
- [5] X. Mougeot, BetaShape: A new code for improved analytical calculations of beta spectra, in: A. Plompen, F. Hamsch, P. Schillebeeckx, W. Mondelaers, J. Heyse, S. Kopecky, P. Siegler, S. Oberstedt (Eds.), *ND 2016: INTERNATIONAL CONFERENCE ON NUCLEAR DATA FOR SCIENCE AND TECHNOLOGY*, Vol. 146 of EPJ Web of Conferences, 2017, international Conference on Nuclear Data for Science and Technology (ND), Bruges, BELGIUM, SEP 11-16, 2016. doi:10.1051/epjconf/201714612015.
- [6] X. Mougeot, Atomic exchange correction in forbidden unique beta transitions, *APPLIED RADIATION AND ISOTOPES* 201 (NOV 2023). doi:10.1016/j.apradiso.2023.111018.
- [7] K. Kossert, X. Mougeot, The importance of the beta spectrum calculation for accurate activity determination of ^{63}Ni by means of liquid

- scintillation counting, APPLIED RADIATION AND ISOTOPES 101 (2015) 40–43. doi:10.1016/j.apradiso.2015.03.017.
- [8] K. Kossert, J. Marganec-Galazka, X. Mougeot, O. J. Naehle, Activity determination of ^{60}Co and the importance of its beta spectrum, APPLIED RADIATION AND ISOTOPES 134 (SI) (2018) 212–218, 21st International Conference on Radionuclide Metrology and its Applications (ICRM), Argentinian Comis Nacl Energia Atomica, Buenos Aires, ARGENTINA, MAY 15-19, 2017. doi:10.1016/j.apradiso.2017.06.015.
- [9] K. Kossert, X. Mougeot, Improved activity standardization of $^{90}\text{Sr}/^{90}\text{Y}$ by means of liquid scintillation counting, APPLIED RADIATION AND ISOTOPES 168 (FEB 2021). doi:10.1016/j.apradiso.2020.109478.
- [10] R. Coulon, J. Hu, TDCRPy: A python package for TDCR measurements, APPLIED RADIATION AND ISOTOPES 214 (DEC 2024). doi:10.1016/j.apradiso.2024.111518.
- [11] M. Loidl, E. Leblanc, M. Rodrigues, J. Bouchard, B. Censier, T. Branger, D. Lacour, Metallic magnetic calorimeters for absolute activity measurement, Journal of Low Temperature Physics 151 (2008) 1055–1060.
- [12] R. Fitzgerald, B. Alpert, D. Becker, D. Bergeron, R. Essex, K. Morgan, S. Nour, G. O’Neil, D. Schmidt, G. Shaw, D. Swetz, R. Verkouteren, D. Yan, Toward a new primary standardization of radionuclide massic activity using microcalorimetry and quantitative milligram-scale samples, Journal of Research of the National Institute of Standards and Technology 126 (01 2021). doi:10.6028/jres.126.048.
- [13] G. B. Kim, L. E. Borg, S. T. P. Boyd, R. H. Cantor, J. D. Despotoulos, O. B. Drury, S. Friedrich, A. Gallant, N. R. Hines, A. Jacobs, I. Jovanovic, K. N. Kmak, A. R. L. Kavner, Y. H. Kim, P. Kunz, A. Kwiatkowski, D. H. Kwon, D. Lee, T. Murböck, N. D. Scielzo, Q. R. Shollenberger, C. K. I. Sio, K. J. Thomas, T. Woody, C. Walls, Absolute decay counting of ^{146}Sm and ^{147}Sm for early solar system chronology, Journal of Low Temperature Physics 209 (5-6) (2022) 824–831. doi:10.1007/s10909-022-02798-6.
URL <GotoISI>://WOS:000833451700001

- [14] O. Nähle, Publishable summary for 20FUN04 PrimA-LTD towards new primary activity tandardisation methods based on low-temperature detectors, Report, EURAMET (2023).
URL [\url{https://prima-ltd.net/wp-content/uploads/2024/02/20FUN04_Publishable_Summary_M27.pdf}](https://prima-ltd.net/wp-content/uploads/2024/02/20FUN04_Publishable_Summary_M27.pdf)
- [15] R. P. Fitzgerald, B. K. Alpert, D. E. Bergeron, M. Carlson, R. Essex, S. Jollota, K. Morgan, S. Muramoto, S. Nour, G. O’Neil, et al., Primary activity measurement of an Am-241 solution using microgram inkjet gravimetry and decay energy spectrometry (2025).
- [16] M. Mueller, M. Rodrigues, J. Beyer, M. Loidl, S. Kempf, Magnetic microcalorimeters for primary activity standardization within the EMPIR project PrimA-LTD, JOURNAL OF LOW TEMPERATURE PHYSICS 214 (3-4, SI) (2024) 263–271. doi:10.1007/s10909-024-03048-7.
- [17] R. Cusnir, P. Froidevaux, P. Carbonez, M. Straub, Solid-phase extraction of ^{225}Ac using ion-imprinted resin and ^{243}Am as a radioactive tracer for internal dosimetry and incorporation measurements, Analytica Chimica Acta 1194 (2022) 339421. doi:<https://doi.org/10.1016/j.aca.2021.339421>.
URL <https://www.sciencedirect.com/science/article/pii/S0003267021012472>
- [18] K. Mathew, C. Ottenfeld, R. Keller, K. Kuhn, J. Fulwyler, Preparation of $^{241}\text{Am}/^{243}\text{Am}$ gravimetric mixtures and development of an isotopic and assay measurement techniques using thermal ionization mass spectrometry, International Journal of Mass Spectrometry 458 (2020) 116430. doi:<https://doi.org/10.1016/j.ijms.2020.116430>.
URL <https://www.sciencedirect.com/science/article/pii/S1387380620303535>
- [19] M. Marouli, S. Pommé, V. Jobbágy, H. Stroh, R. Van Ammel, A. Fankhauser, R. Jakopič, S. Richter, Y. Aregbe, M. Crozet, et al., Absolute and relative measurement of the ^{243}Am half-life, Journal of Radioanalytical and Nuclear Chemistry 326 (2020) 1785–1793.
- [20] E. Browne, J. Tuli, Nuclear data sheets for $A = 239$, Nuclear Data Sheets 122 (2014) 293–376. doi:<https://doi.org/10.1016/j.nds.2014.11.003>.

URL <https://www.sciencedirect.com/science/article/pii/S0090375214006693>

- [21] M. Bodine, et al., Standardization of Am-243, APPLIED RADIATION AND ISOTOPES (these proceedings).
- [22] K. E. Koehler, Low temperature microcalorimeters for decay energy spectroscopy, Applied Sciences 11 (9) (2021). doi:10.3390/app11094044.
- [23] A. Kavner, Q. Shollenberger, K. Kmak, L. Borg, S. Boyd, J. Despotopoulos, O. Drury, I. Jovanovic, S. Friedrich, A. Gallant, I. Kim, Y. Kim, P. Kunz, A. Kwiatkowski, D. Kwon, D. Lee, N. Scielzo, G. Kim, Absolute decay counting of ^{146}Sm with 4π cryogenic microcalorimetry, Nuclear Instruments and Methods in Physics Research Section A: Accelerators, Spectrometers, Detectors and Associated Equipment 1065 (2024) 169462. doi:<https://doi.org/10.1016/j.nima.2024.169462>.
URL <https://www.sciencedirect.com/science/article/pii/S0168900224003887>
- [24] M. Rodrigues, M. Loidl, S. Pierre, Determination of absolute Np L x-ray emission intensities from ^{241}Am decay using a metallic magnetic calorimeter, METROLOGIA 60 (2) (APR 1 2023). doi:10.1088/1681-7575/acb99f.
- [25] M. Loidl, J. Beyer, L. Bockhorn, C. Enss, S. Kempf, K. Kossert, R. Mariam, O. Nähle, M. Paulsen, P. Ranitzsch, M. Rodrigues, M. Schmidt, Beta spectrometry with metallic magnetic calorimeters in the framework of the European EMPIR project MetroBeta, Applied Radiation and Isotopes 153 (2019). doi:ARTN 108830 10.1016/j.apradiso.2019.108830.
URL <GotoISI>://WOS:000520020400028
- [26] D. Deptuck, M. Lowry, I. Girit, Cryogenic micro-calorimeters for low energy beta spectroscopy, Journal of Low Temperature Physics 93 (1993) 269–274.
- [27] L. Erhardt, D. Deptuck, J. Harrison, Transition-edge microcalorimeter for tritium beta decay, Nuclear Instruments and Methods in Physics Research Section A: Accelerators, Spectrometers, Detectors and Associated

Equipment 444 (1) (2000) 92–95. doi:[https://doi.org/10.1016/S0168-9002\(99\)01336-4](https://doi.org/10.1016/S0168-9002(99)01336-4).

URL <https://www.sciencedirect.com/science/article/pii/S0168900299013364>

- [28] M. Rodrigues, M. Laarraj, M. Loidl, X.-F. Navick, L. Ferlazzo, Preparation of drop-deposited sources in 4π absorbers for total decay energy spectrometry, *JOURNAL OF LOW TEMPERATURE PHYSICS* 199 (1-2, SI) (2020) 461–466. doi:10.1007/s10909-020-02410-9.
- [29] A. S. Hoover, E. M. Bond, M. P. Croce, T. G. Holesinger, G. J. Kunde, M. W. Rabin, L. E. Wolfsberg, D. A. Bennett, J. P. Hays-Wehle, D. R. Schmidt, D. Swetz, J. N. Ullom, Measurement of the $^{240}\text{Pu}/^{239}\text{Pu}$ mass ratio using a transition-edge-sensor microcalorimeter for total decay energy spectroscopy, *Analytical Chemistry* 87 (7) (2015) 3996–4000, pMID: 25723106. arXiv:<https://doi.org/10.1021/acs.analchem.5b00195>, doi:10.1021/acs.analchem.5b00195.
URL <https://doi.org/10.1021/acs.analchem.5b00195>
- [30] A. Kaur, L. Chambon, M. Loidl, V. Lourenço, M. Rodrigues, M.-L. Zahir, Determination of fractional electron capture probabilities of ^{59}Ni by means of Metallic Magnetic Calorimeters, *Journal of Low Temperature Physics* 218 (1) (2025) 29–38.
- [31] J. C. Weber, K. M. Morgan, D. Yan, C. G. Pappas, A. L. Wessels, G. C. O’Neil, D. A. Bennett, G. C. Hilton, D. S. Swetz, J. N. Ullom, D. R. Schmidt, Development of a transition-edge sensor bilayer process providing new modalities for critical temperature control, *Superconductor Science and Technology* 33 (11) (2020) 115002. doi:10.1088/1361-6668/abb206.
URL <https://dx.doi.org/10.1088/1361-6668/abb206>
- [32] K. M. Morgan, Hot science with cool sensors, *Physics Today* 71 (8) (2018) 28–34. doi:10.1063/pt.3.3995.
- [33] A. D. Tollefson, C. M. Smith, M. H. Carpenter, M. P. Croce, M. E. Fassbender, K. E. Koehler, L. M. Lilley, E. M. O’Brien, D. R. Schmidt, B. W. Stein, J. N. Ullom, M. D. Yoho, D. J. Mercer, Measurement of (^{227}Ac) impurity in (^{225}Ac) using decay energy spectroscopy, *Appl*

Radiat Isot 172 (2021) 109693. doi:10.1016/j.apradiso.2021.109693.
URL <https://www.ncbi.nlm.nih.gov/pubmed/33774323>

- [34] C. Whitford, W. B. Tiest, A. Holland, Practical considerations in optimal filtering of TES signals, *Nuclear Instruments and Methods in Physics Research Section A: Accelerators, Spectrometers, Detectors and Associated Equipment* 520 (1-3) (2004) 592–594.
- [35] M. T. Ceballos, N. Cardiel, B. Cobo, P. Peille, S. J. Smith, M. Witthoef, M. Durkin, When less is more: the truncation of the optimal filter to reconstruct events in X-IFU/Athena-like TES detectors, in: *Space Telescopes and Instrumentation 2022: Ultraviolet to Gamma Ray*, Vol. 12181, SPIE, 2022, pp. 1061–1069.
- [36] H. Tan, W. Hennig, W. K. Warburton, W. B. Doriese, C. A. Kilbourne, Development of a real-time pulse processing algorithm for tes-based x-ray microcalorimeters, *IEEE Transactions on Applied Superconductivity* 21 (3) (2011) 276–280. doi:10.1109/TASC.2010.2082473.
- [37] B. K. Alpert, W. B. Doriese, J. W. Fowler, J. N. Ullom, Predicted energy resolution of a running-sum algorithm for microcalorimeters, *Journal of Low Temperature Physics* 167 (2012) 582–587.
- [38] R. M. Verkouteren, J. R. Verkouteren, Inkjet metrology II: resolved effects of ejection frequency, fluidic pressure, and droplet number on reproducible drop-on-demand dispensing, *Langmuir* 27 (15) (2011) 9644–53. doi:10.1021/la201728f.
URL <https://www.ncbi.nlm.nih.gov/pubmed/21667998>
- [39] S. P. Jollota, D. E. Bergeron, R. M. Verkouteren, S. Nour, R. P. Fitzgerald, O. Kwon, J. L. Radtke, B. P. Bednarz, B. W. Miller, L. A. DeWerd, Gravimetric drop-on-demand inkjet deposition for imaging phantoms with traceable activity, *Applied Radiation and Isotopes* 218 (2025) 111683. doi:<https://doi.org/10.1016/j.apradiso.2025.111683>.
URL <https://www.sciencedirect.com/science/article/pii/S0969804325000284>
- [40] B. Zimmerman, R. Collé, J. Cessna, Construction and implementation of the NIST triple-to-double coincidence ratio (TDCR) spectrometer, *Applied Radiation and Isotopes* 60 (2)

- (2004) 433–438, proceedings of the 14th International Conference on Radionuclide Metrology and its Applications, ICRM 2003. doi:<https://doi.org/10.1016/j.apradiso.2003.11.055>.
URL <https://www.sciencedirect.com/science/article/pii/S096980430300349X>
- [41] C. Le-Bret, M. Loidl, M. Rodrigues, X. Mougeot, J. Bouchard, Study of the influence of the source quality on the determination of the shape factor of beta spectra, *Journal of Low Temperature Physics* 167 (2012) 985–990.
- [42] M. Carlson, R. P. Fitzgerald, G. O’Neil, D. Schmidt, Characterization of transition edge sensors for decay energy spectrometry, *Journal of Low Temperature Physics* 216 (2024). doi:<https://doi.org/10.1007/s10909-024-03135-9>.
URL https://tsapps.nist.gov/publication/get_pdf.cfm?pub_id=956930
- [43] S. Pomme, R. Fitzgerald, J. Keightley, Uncertainty of nuclear counting, *Metrologia* 52 (3) (2015) S3–S17. doi:<https://doi.org/10.1088/0026-1394/52/3/s3>.
URL <GotoISI>://WOS:000354997100002
- [44] D. E. Bergeron, R. Essex, S. Nour, G. A. Shaw, R. M. Verkouteren, R. P. Fitzgerald, Gravimetric deposition of microliter drops with radiometric confirmation, *Applied Radiation and Isotopes* 201 (2023) 111025. doi:<https://doi.org/10.1016/j.apradiso.2023.111025>.
URL <https://www.sciencedirect.com/science/article/pii/S0969804323003780>
- [45] G. Bortels, P. Collaers, Analytical function for fitting peaks in alpha-particle spectra from Si detectors, *International Journal of Radiation Applications and Instrumentation. Part A. Applied Radiation and Isotopes* 38 (10) (1987) 831–837. doi:[https://doi.org/10.1016/0883-2889\(87\)90180-8](https://doi.org/10.1016/0883-2889(87)90180-8).
URL <https://www.sciencedirect.com/science/article/pii/0883288987901808>
- [46] S. Agostinelli, J. Allison, K. Amako, J. Apostolakis, H. Araujo, P. Arce, M. Asai, D. Axen, S. Banerjee, G. Barrand, F. Behner, L. Bellagamba,

J. Boudreau, L. Broglia, A. Brunengo, H. Burkhardt, S. Chauvie, J. Chuma, R. Chytracek, G. Cooperman, G. Cosmo, P. Degtyarenko, A. Dell'Acqua, G. Depaola, D. Dietrich, R. Enami, A. Feliciello, C. Ferguson, H. Fesefeldt, G. Folger, F. Foppiano, A. Forti, S. Garelli, S. Giani, R. Giannitrapani, D. Gibin, J. Gómez Cadenas, I. González, G. Gracia Abril, G. Greeniaus, W. Greiner, V. Grichine, A. Grossheim, S. Guatelli, P. Gumplinger, R. Hamatsu, K. Hashimoto, H. Hasui, A. Heikkinen, A. Howard, V. Ivanchenko, A. Johnson, F. Jones, J. Kallenbach, N. Kanaya, M. Kawabata, Y. Kawabata, M. Kawaguti, S. Kelner, P. Kent, A. Kimura, T. Kodama, R. Kokoulin, M. Kossov, H. Kurashige, E. Lamanna, T. Lampén, V. Lara, V. Lefebure, F. Lei, M. Liendl, W. Lockman, F. Longo, S. Magni, M. Maire, E. Medernach, K. Minamimoto, P. Mora de Freitas, Y. Morita, K. Murakami, M. Nagamatu, R. Nartallo, P. Nieminen, T. Nishimura, K. Ohtsubo, M. Okamura, S. O'Neale, Y. Oohata, K. Paech, J. Perl, A. Pfeiffer, M. Pia, F. Ranjard, A. Rybin, S. Sadilov, E. Di Salvo, G. Santin, T. Sasaki, N. Savvas, Y. Sawada, S. Scherer, S. Sei, V. Sirotenko, D. Smith, N. Starkov, H. Stoecker, J. Sulkimo, M. Takahata, S. Tanaka, E. Tcherniaev, E. Safai Tehrani, M. Tropeano, P. Truscott, H. Uno, L. Urban, P. Urban, M. Verderi, A. Walkden, W. Wander, H. Weber, J. Wellisch, T. Wenaus, D. Williams, D. Wright, T. Yamada, H. Yoshida, D. Zschesche, Geant4 - a simulation toolkit, *Nuclear Instruments and Methods in Physics Research Section A: Accelerators, Spectrometers, Detectors and Associated Equipment* 506 (3) (2003) 250–303. doi:[https://doi.org/10.1016/S0168-9002\(03\)01368-8](https://doi.org/10.1016/S0168-9002(03)01368-8).
 URL <https://www.sciencedirect.com/science/article/pii/S0168900203013688>

- [47] G. Sibbens, T. Altzitzoglou, Preparation of radioactive sources for radionuclide metrology, *Metrologia* 44 (4) (2007) S71.
- [48] M. Niedźwiecki, M. Meller, P. Pietrzak, System identification based approach to dynamic weighing revisited, *Mechanical Systems and Signal Processing* 80 (2016) 582–599. doi:<https://doi.org/10.1016/j.ymssp.2016.04.007>.
 URL <https://www.sciencedirect.com/science/article/pii/S0888327016300450>
- [49] R. D. Horansky, D. A. Bennett, D. R. Schmidt, B. L. Zink,

- J. N. Ullom, Identification and elimination of anomalous thermal decay in gamma-ray microcalorimeters, *Applied Physics Letters* 103 (21) (2013) 212602. arXiv:https://pubs.aip.org/aip/apl/article-pdf/doi/10.1063/1.4830373/13557108/212602_1_online.pdf, doi:10.1063/1.4830373.
URL <https://doi.org/10.1063/1.4830373>
- [50] S. J. Smith, J. S. Adams, S. R. Bandler, J. A. Chervenak, A. M. Datesman, M. E. Eckart, F. M. Finkbeiner, R. Hummatov, R. L. Kelley, C. A. Kilbourne, et al., Multiabsorber transition-edge sensors for x-ray astronomy, *Journal of Astronomical Telescopes, Instruments, and Systems* 5 (2) (2019) 021008–021008.
- [51] T. Tsuruta, N. Iyomoto, Y. Matsumi, Y. Tagawa, H. Fujita, M. Kihara, N. Yamasaki, T. Hayashi, Y. Yagi, K. Mitsuda, et al., Development of TES microcalorimeters with serpentine absorbers for two-dimensional position detection, *IEEE Transactions on Applied Superconductivity* (2025).
- [52] K. Irwin, An application of electrothermal feedback for high resolution cryogenic particle detection, *Applied Physics Letters* 66 (15) (1995) 1998–2000.